Characterization of the unoccupied and partially occupied states of TTF-TCNQ by XANES and first-principles calculations

J. Fraxedas,[1] Y. J. Lee,[2] I. Jiménez,[3] R. Gago,[4] R. M. Nieminen,[2] P. Ordejón,[1] and E. Canadell[1]
[1]*Institut de Ciència de Materials de Barcelona (CSIC), Campus de la U.A.B., 08193 Bellaterra, Spain*
[2]*COMP/Laboratory of Physics, Helsinki University of Technology, P.O.Box 1100, FIN-02015 HUT, Finland*
[3]*Instituto de Ciencia y Tecnología de Polímeros (CSIC), 28006 Madrid, Spain*
[4]*Forschungszentrum Rossendorf e.V. PF-510119, 01314 Dresden, Germany*
(Received 17 July 2003; published 21 November 2003)

We report a combined experimental and theoretical study of the unoccupied electronic states of the neutral molecular organic materials TTF (tetrathiafulvalene) and TCNQ (7,7,8,8-tetracyano-*p*-quinodimethane) and of the one-dimensional metallic charge transfer salt TTF-TCNQ. The experimental density of states (DOS) is obtained by x-ray absorption near edge spectroscopy (XANES) with synchrotron light and the predicted DOS by means of first-principles density functional theory calculations. Most of the experimentally derived element-specific XANES features can be associated to molecular orbitals of defined symmetry. Because of the planar geometry of the TTF and TCNQ molecules and the polarization of the synchrotron light, the energy dependent σ or π character of the orbitals can be inferred from angular dependent XANES measurements. The present work represents the state of the art analysis of the XANES spectra of this type of materials and points out the need for additional work in order to elucidate the governing selection rules in the excitation process.

DOI: 10.1103/PhysRevB.68.195115 PACS number(s): 71.20.Rv, 71.15.Mb, 61.10.Ht

I. INTRODUCTION

The successful marriage between the tetrathiafulvalene (TTF, $C_6S_4H_4$) donor and the 7,7,8,8-tetracyano-*p*-quinodimethane (TCNQ, $C_{12}N_4H_4$) acceptor, which led to the first truly molecular metal,[1] opened a vast area of research which thirty years later remains as lively and exciting as ever.[2] TTF-TCNQ exhibits a monoclinic crystal structure[3] built up from parallel segregated stacks of donors (TTF) and acceptors (TCNQ) (see Fig. 1). Due to the π-π interactions along the stacks (*b* direction) and the weak interactions between molecular chains, the electrical conductivity is highly anisotropic with typical values of $\sigma_b \sim 600$–$900\ \Omega^{-1}\,\mathrm{cm}^{-1}$ and $\sigma_b/\sigma_a \sim 10^3$ at room temperature, where σ_a and σ_b stand for the conductivity along the *a* and *b* axes, respectively, increasing to a maximum value close to 6×10^3 near 60 K.[4] TTF-TCNQ is thus a quasi-one-dimensional metal and exhibits a series of transitions at 54, 49, and 38 K, which successively destroy the metallic conductivity of the TCNQ and TTF chains.[5] The discovery of TTF-TCNQ and its remarkable low-temperature behavior triggered an enormous interest on the physics of molecular conductors which soon led to the discovery of superconductivity in the molecular solid $(TMTSF)_2PF_6$ (TMTSF: tetramethyltetraselenenafulvalene).[6] Since then molecular conductors have provided a seemingly endless series of exciting discoveries and TTF-TCNQ has remained as one of the emblems of the field. In fact, it is one of the materials best suited for the exploration of the physics of one-dimensional (1D) materials.[5]

Despite the continued attention devoted to the physical characterization of TTF-TCNQ, some aspects of its electronic structure still remain ambiguous. Although some recent works on the experimental determination of the energy dispersion of the occupied states by means of high resolution angle resolved photoemission spectroscopy (ARPES) have been published,[7–9] little is known concerning the unoccupied levels region of the band structure. Information on the density of unoccupied electronic states of TTF-TCNQ has been obtained with inelastic electron scattering spectroscopy (IESS) in transmission mode with 300 keV electrons.[10] The surfaces of molecular organic materials are in general very sensitive to irradiation, so that impinging electrons may induce irreversible damage. Results derived from inverse photoemission spectroscopy (IPS) might be also questionable

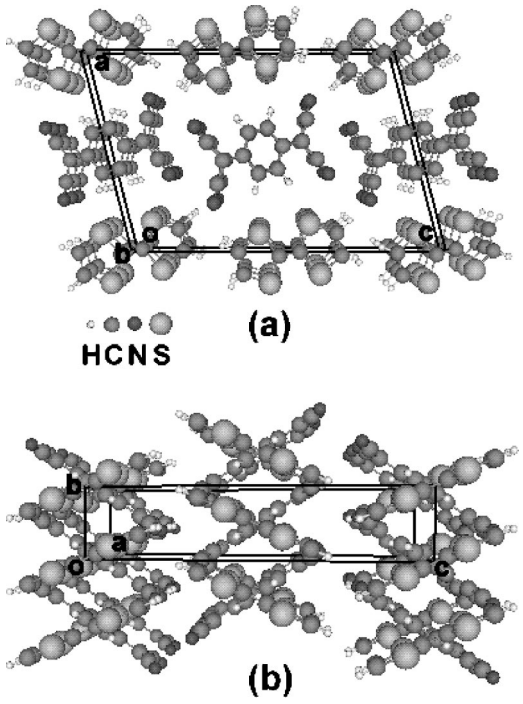

FIG. 1. Crystal structure of TTF-TCNQ: (a) view along the *b* axis and (b) view along the direction perpendicular to the *bc* plane.

unless low energy electrons (around 10–20 eV) and low beam currents are used as in low energy electron diffraction (LEED) experiments.[11] Since molecular materials are less sensitive to x-ray photons, x-ray absorption near edge spectroscopy (XANES) represents an interesting alternative. This technique is based on the induction of intra-atomic interband transitions from core levels to empty states caused by incident x rays of sufficient energy.[12] Therefore, the partial (element selective) density of unoccupied states corresponding to the electronic excited state with one core hole, which can be used in a first approximation as the image of the unoccupied states in the electronic ground state, is obtained.[13] A closely related technique, which would give complementary information, is angle resolved constant initial state (ARCIS) spectroscopy.[14] Here we report a XANES study of the density of unoccupied states of TTF-TCNQ salt as well as of neutral TTF and TCNQ. These results are analyzed on the basis of a comparison with first-principles density functional theory (DFT) calculations for the three materials, which also allow us to discuss in detail the nature of the partially filled bands of TTF-TCNQ. Thus, we believe that the present work provides the most complete description of the electronic structure of these materials reported so far.

II. EXPERIMENTAL

Thin TTF-TCNQ films (thickness ~ 1 μm) have been obtained by thermal sublimation in high vacuum ($\sim 10^{-6}$ mbar) of recrystallized TTF-TCNQ powder. *Ex situ* cleaved KCl(001) surfaces were used as substrates, held at room temperature during deposition. The films are oriented with their molecular *ab* planes parallel to the substrate surface and consist of highly oriented and strongly textured rectangular-shaped microcrystals, with their *a* and *b* axes parallel to both [110] and $[\bar{1}10]$ substrate directions, respectively, due to the cubic symmetry of the substrate.[15] The mean length of the microcrystals along their long axis (*b* direction) is around 1.5 μm. Thin films of neutral TTF and TCNQ were prepared from their microcrystalline powders by suspension in ethanol and by stirring and deposition on a silicon wafer immersed in the suspension. The information on the spatial distribution of empty states is obtained by performing XANES measurements at different angles of incidence of the x-ray light, taking advantage of the intrinsic linear polarization of synchrotron radiation. The example of graphite is illuminating, since from initial *s* states σ (i.e., symmetric with respect to the molecular plane) or π (i.e., antisymmetric with respect to the molecular plane) final states are selected when the light polarization vector **E** lies parallel or perpendicular to the basal plane, respectively.[16] In general, intramolecular transitions, i.e., $1s \rightarrow \pi^*$ and $1s \rightarrow \sigma^*$, in molecules containing C, N, and O atoms are strongly polarized.[17] The XANES measurements were performed at the SACEMOR endstation (beamline SA72) of the *Laboratoire pour l' Utilisation du Rayonnement Electromagnetique* (LURE) in Orsay, France and at the beamline 8.2 of the Stanford Synchrotron Radiation Laboratory (SSRL) in Stanford, CA. The data were acquired in the total electron yield mode by measuring with an ammeter the current drain to ground. The signal was normalized to the simultaneously recorded photocurrent from a gold-covered grid.

III. COMPUTATIONAL DETAILS

The present calculations were carried out using a numerical atomic orbitals DFT (Ref. 18) approach, which has been recently developed and designed for efficient calculations in large systems and implemented in the SIESTA code.[19] We have used the generalized gradient approximation to the exchange correlation energy and, in particular, the functional of Perdew, Burke, and Ernzerhof.[20] Only the valence electrons are considered in the calculation, with the core being replaced by norm-conserving scalar relativistic pseudopotentials[21] factorized in the Kleinman-Bylander form.[22] For the nonlinear core-valence interaction, the partial-core correction scheme was used for all elements except for hydrogen.[23] We have used the following type of basis set: triple-ζ for the *s* orbitals of S, N, and C atoms, triple-ζ plus single polarization functions for the *s* orbital of H, double-ζ plus single polarization functions for the *p* orbitals of S, N, and C, as obtained with an energy shift of 5 meV.[24] The integrals of the self-consistent terms of the Kohn-Sham Hamiltonian are obtained with the help of a regular real space grid in which the electron density is projected. The grid spacing is determined by the maximum kinetic energy of the plane waves that can be represented in that grid. In the present work, we used a cutoff of 250 Ry. The Brillouin zone (BZ) was sampled using grids of $3\times9\times2$, $4\times7\times2$, and $2\times3\times1$ *k* points[25] for the determination of density matrices and partial densities of states of TTF-TCNQ, TTF, and TCNQ, respectively. Sets of 23 000, 24 000, and 10 000 *k* points were used for determination of the total densities of states of TTF-TCNQ, TTF, and TCNQ, respectively. The above-mentioned methods have been applied to the electronic structure study of other organic conductors, and proved to give highly accurate results.[26]

IV. RESULTS AND DISCUSSION

A. Theoretical band structure close to the Fermi level

Before looking at the unoccupied levels region of the band structure let us consider how the present calculations describe the region around the Fermi level. Because of the molecular nature and the relatively large unit cell, the correct description of the electronic structure of TTF-TCNQ (as most of the molecular conductors) is still a challenge from the computational viewpoint. Initial first-principles calculations by Starikov[27] as well as Kasowski *et al.*[28] are in contradiction with some of the symmetry requirements of the crystal structure and thus cannot be considered as satisfactory. Very recently, Ishibashi *et al.*[29] as well as Claessen *et al.*[8,30] have reported band calculations by plane-wave pseudopotential methods for TTF-TCNQ, although these authors only consider in detail the region near the Fermi level. Before studying the XANES spectra it is thus interesting to consider how the present atomic orbitals band calculations compare with them for this region as well as its significance in discussing very recent photoemission studies.

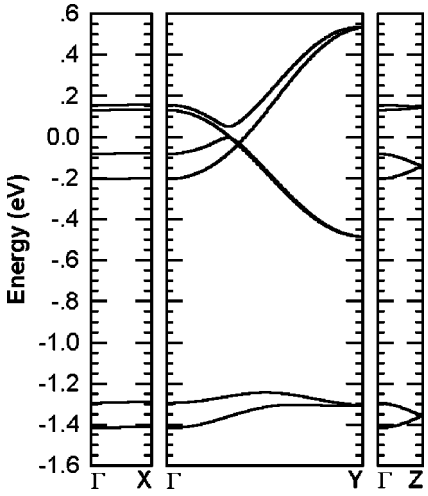

FIG. 2. Band structure near the Fermi level for the room temperature and ambient pressure structure of TTF-TCNQ. $\Gamma=(0,0,0)$, $X=(1/2,0,0)$, $Y=(0,1/2,0)$, and $Z=(0,0,1/2)$ in units of the monoclinic reciprocal lattice vectors. Energy is given relative to the Fermi level.

Shown in Fig. 2 is the calculated band structure near the Fermi level (origin of energies) along the a^* (Γ to X), b^* (Γ to Y), and c^* (Γ to Z) directions of the reciprocal lattice. The room temperature and ambient pressure experimental structure was used in these computations.[3] There are two pairs of bands in the vicinity of the Fermi level. The bands pair up at the Y and Z points because there are two symmetry related chains of each type in the unit cell. The two upper bands at Γ, located at $+0.12$ and $+0.15$ eV, are built from the TTF highest occupied molecular orbital (HOMO). In contrast, the two lower bands at Γ are built from the TCNQ lowest unoccupied orbital (LUMO), and located at -0.08 and -0.20 eV. This splitting, 0.12 eV, means that the TCNQ chains are not completely isolated within the solid and interact along the c direction (see Figs. 1 and 2). Although this coupling is not very strong, it may have some influence in the detailed shape of the Fermi surface because it is kept in the region of the Fermi level. The two TTF HOMO bands are practically degenerate all over the Brillouin zone except for the region of the weakly avoided crossing around the Fermi level. The bandwidth of the TTF HOMO and TCNQ LUMO bands along the chain direction are not very different: 0.62 and 0.73 eV, respectively. The value for the TCNQ LUMO bands is in reasonably good agreement with experimental estimations which are around 0.7–0.8 eV.[5,31] However, the value for the TTF HOMO bands does not seem to follow commonly accepted ideas according to which the dispersion should be clearly smaller than that of the TCNQ LUMO bands. Experimental estimations suggest values around 0.4–0.45 eV.[5,31] Let us note, however, that high resolution photoemission experiments have suggested values which are considerably larger for both TTF HOMO (0.95 eV) and TCNQ LUMO (2.5 eV).[7]

Analysis of the calculated PDOS shows that 61% of the electron density associated with the TTF HOMO originates from the four sulfur atoms, 22% from the two central carbon atoms, and 17% from the four outer carbon atoms. That is,

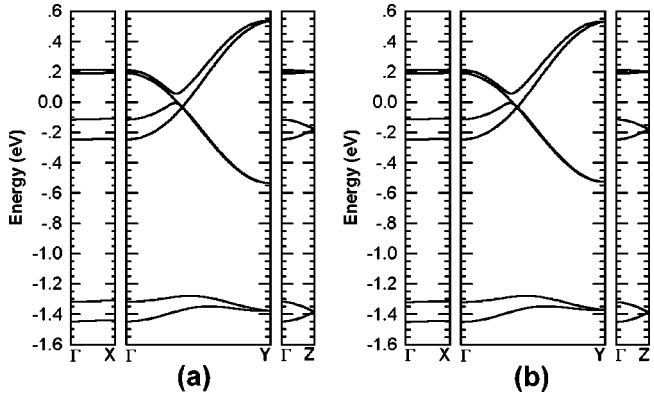

FIG. 3. Band structure calculated using the 60 K (a) and room temperature and 4.5 kbar (b) crystal structures of TTF-TCNQ. $\Gamma=(0,0,0)$, $X=(1/2,0,0)$, $Y=(0,1/2,0)$, and $Z=(0,0,1/2)$ in units of the monoclinic reciprocal lattice vectors. Energy is given relative to the Fermi level.

the contribution of each of the four sulfur atoms is approximately 1.4 times larger than that of each of the central carbon atoms and approximately 3.7 times that of each of the outer carbon atoms, in agreement with usual molecular orbital ideas. As it will be shown later, the larger participation of the sulfur atoms in the HOMO will have direct consequences for the XANES spectra. The same analysis shows that the TCNQ LUMO is much more uniformly distributed along the molecule.

Our results for the band structures are almost identical to those of previous work by Ishibashi *et al.*[29] and Claessen *et al.*,[8,30] despite technical differences between the three calculations (Ishibashi *et al.* use LDA and GGA within a plane-wave pseudopotential method, Claessen *et al.* use LDA within the LAPW approach, and we use GGA with atomic orbitals and pseudopotentials). Let us note, however, that the use of atomic orbitals in our approach requires a considerably smaller computational cost.

We have also considered how this description of the electronic structure depends on pressure and temperature. Thus, we have carried out computations using the crystal structure at 60 K,[32] nearby the Peierls transition, as well as at room temperature and 4.6 kbar.[33] The calculated band structures are shown in Fig. 3. Except for an expected increase in the dispersion along the chain direction (of the order of 15% for TTF and 7% for TCNQ for both the above-mentioned pressure and temperature variations), there are no noticeable changes in the band structure. We have also carried out a minimization of the structure using the cell constants at room temperature and ambient pressure, and the results are very similar. Thus, we conclude that the present view of the partially filled bands of TTF-TCNQ is quite stable to temperature and pressure effects except for the expected slight increase in the dispersion along the chains direction. The main difference between the DFT description and the currently accepted view of these partially filled bands is the larger dispersion of the TTF HOMO bands and the slightly lower one dimensionality of the TCNQ bands.

There is also a difference in what concerns the charge transfer ρ. X-ray diffuse scattering studies have shown that

$\rho = 0.55$ electrons/molecule at room temperature and 0.59 at low temperature near the Peierls transition.[34] In contrast, the calculated ρ at room temperature is 0.74 and practically does not change with pressure or temperature. Similar values (0.70–0.72) were reported by Ishibashi *et al.*[29] It is not clear if this overestimation of ρ and the larger calculated dispersion for the TTF HOMO bands are related. Let us note that $4k_f$ (k_f is the Fermi wave vector) fluctuations associated with the TTF chains have been observed in x-ray diffuse scattering experiments[34] suggesting that electron correlations are important for TTF but less for TCNQ. Thus it may well be that both LDA and GGA approaches to DFT lead to a slightly better description of the TCNQ chains than the TTF ones. However, let us note that just a shift of the order of 50 meV of the TTF HOMO bands with respect to the TCNQ LUMO ones would lead to the correct ρ so that for the current purposes the disagreement is not really significant.

Finally, we also considered the possible effect of the surface structural relaxation on the band structure by carrying out a model calculation for the *ab*-plane relaxation. A geometry optimization of the outer layer while keeping the underlying ones fixed at the bulk geometry was carried out. The geometrical changes are not large and affect more the TTF than the TCNQ. They both change their inclination with respect to the *ab* plane but none of the two molecules undergo any rotational motion along the long molecular axis. Changes in the band dispersion along the chain direction are small, of the same order but slightly smaller than those due to thermal contraction or pressure reported above. The component of the Fermi wave vector along b^* practically does not change. Consequently, at least in what concerns the *ab* plane, no noticeable changes in ρ are expected at the surface due to the structural relaxation, in line with recent scanning tunneling microscopy results performed at cryogenic temperatures under ultrahigh vacuum.[35]

B. Electronic structure of unoccupied states

The crystal structure of neutral TTF ($a = 7.36$ Å, $b = 4.023$ Å, $c = 13.922$ Å, $\beta = 101.42°$) (Ref. 36) and TCNQ ($a = 8.906$ Å, $b = 7.060$ Å, $c = 16.395$ Å, $\beta = 98.54°$) (Ref. 37) are shown in Figs. 4(a) and 4(b) and Figs. 5(a) and 5(b), respectively. Note that there are two molecules per repeat unit of the crystal structure for neutral TTF but four for neutral TCNQ. TTF contains one-dimensional stacks along the *b* direction where every successive molecule slides along the long molecular axis. These stacks are similar to those found in TTF-TCNQ. In contrast, neutral TCNQ does not really contain one-dimensional stacks as in TTF-TCNQ (see Fig. 1) but two-dimensional ones in the *ab* planes [see Figs. 5(a) and 5(b)]. The calculated band structures are reported in Figs. 4(c) and 5(c) for TTF and TCNQ, respectively. The calculated band structure for TTF-TCNQ in the same energy range is shown in Fig. 6(a). Note that the two TTF HOMO bands as well as the four TCNQ LUMO bands are well separated from the bands above and this leads to a well defined energy gap between the partially filled and empty bands of the TTF-TCNQ. Whereas the TTF HOMO bands are practically degenerate in TTF-TCNQ, they are not in neutral TTF, i.e., the interchain interactions are larger in the neutral compound. The dispersion of these bands along the chain direction is not very different in TTF and TTF-TCNQ.

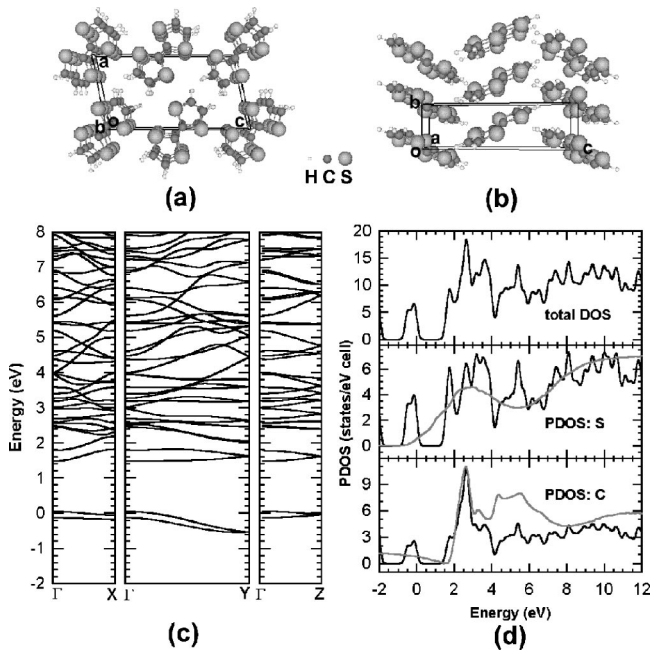

FIG. 4. View along the *b* axis (a) and along the direction perpendicular to the *bc* plane (b) of the crystal structure of neutral TTF. (c) Band structure of TTF where $\Gamma = (0,0,0)$, $X = (1/2,0,0)$, $Y = (0,1/2,0)$, and $Z = (0,0,1/2)$ in units of the monoclinic reciprocal lattice vectors. (d) Total DOS calculated for neutral TTF and PDOS for the sulfur and carbon atoms (black lines). The S2*p* and C1*s* XANES spectra of TTF (gray lines) are superposed to the PDOS of S and C, respectively. The energy is given relative to the HOMO maximum.

In contrast, the structural origin of the spreading of the TCNQ LUMO levels is very different in the neutral and the salt compounds. Consequently, the appearance of the TCNQ LUMO bands is very different in the neutral and the salt compounds. However, note that the total spread of these levels in the neutral is only one third smaller than in the salt and, as far as the gross features of the density of states are concerned, the differences between the neutral and the salt are not very significant (see below). Similar observations apply for the upper bands and make directly comparable the XANES results for TTF-TCNQ and those for TCNQ. The calculated total DOS and PDOS for the relevant atoms of TTF-TCNQ, TTF, and TCNQ are reported in Figs. 6(b), 4(d), and 5(d), respectively, and compared to the appropriate experimental XANES data. The S2*p*, C1*s*, and N1*s* XANES spectra for TTF-TCNQ, TTF, and TCNQ are also shown in Fig. 7 where the relevant molecular orbitals of TTF and TCNQ associated with the different features of the spectra are indicated. These molecular orbitals are schematically shown in Figs. 8 (TTF) and 9 (TCNQ). The energy values associated with the orbitals of Figs. 8 and 9 are those calculated for a single molecule with the same geometry as for the neutral solid. The symmetry labels are those appropriate for

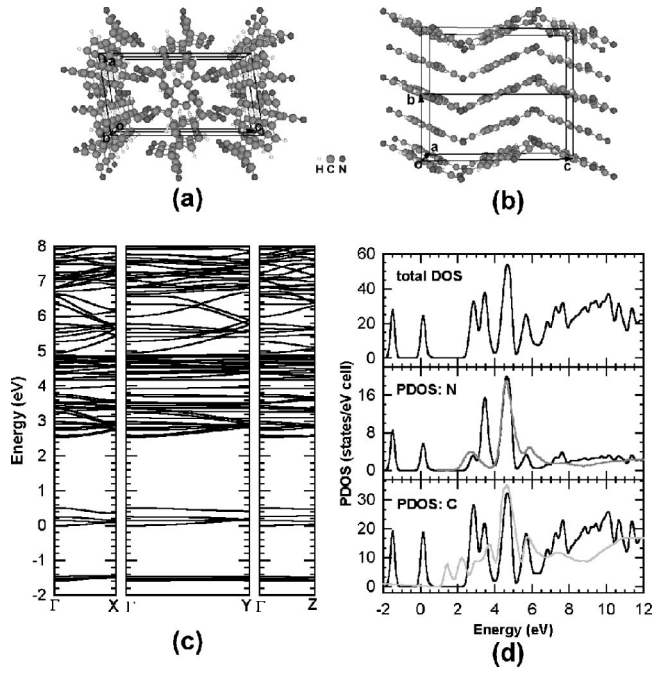

FIG. 5. View along the *b* axis (a) and along the direction perpendicular to the *bc* plane (b) of the crystal structure of neutral TCNQ. (c) Band structure of TCNQ where $\Gamma=(0,0,0)$, $X=(1/2,0,0)$, $Y=(0,1/2,0)$, and $Z=(0,0,1/2)$ in units of the monoclinic reciprocal lattice vectors. (d) Total DOS calculated for neutral TCNQ and PDOS for the nitrogen and carbon atoms (black lines). The N1*s* and C1*s* XANES spectra of TCNQ (gray lines) are superposed to the PDOS of N and C, respectively. The energy is given relative to the LUMO minimum.

idealized D_{2h} symmetry. For simplicity, the sulfur *d* orbital contributions have not been shown in these schematic drawings.

1. TTF-derived spectral features

Let us start considering neutral and charged TTF. The experimental spectra for S2*p* corresponding to neutral TTF

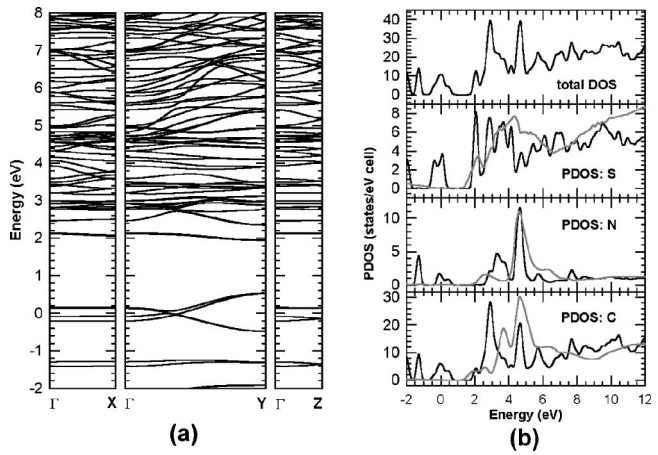

FIG. 6. (a) Band structure calculated for the room temperature structure of TTF-TCNQ where $\Gamma=(0,0,0)$, $X=(1/2,0,0)$, $Y=(0,1/2,0)$, and $Z=(0,0,1/2)$ in units of the monoclinic reciprocal lattice vectors. (b) Total DOS calculated for TTF-TCNQ and PDOS for the sulfur, carbon, and nitrogen atoms (black lines). The S2*p*, N1*s* and C1*s* XANES spectra of TTF-TCNQ (gray lines) are superposed to the PDOS of S, N, and C, respectively. Energy is given relative to the Fermi level.

is not quite structured whereas that for charged TTF is. The S2*p* lines are composed of two spin-orbit splitted components $2p_{3/2}$ and $2p_{1/2}$ separated by 1.1 eV,[38] so that the S2*p* XANES spectra consists of the superposition of both contributions. The opposite trend is observed for N1*s* in TCNQ, with narrower spectral lines in the neutral state as compared to the TTF-TCNQ salt. On the other hand C1*s* XANES spectra show well-defined features for both neutral and charged TTF and TCNQ. The explanation indeed stems from the charge transferred upon formation of the TTF-TCNQ compound from the donor TTF to the acceptor TCNQ. The extra charge that is allocated within the TCNQ electronic structure broadens its electronic levels, whereas the loss of charge in TTF narrows the line shape of the corresponding states. The narrowing of the TTF spectral width corresponds to an in-

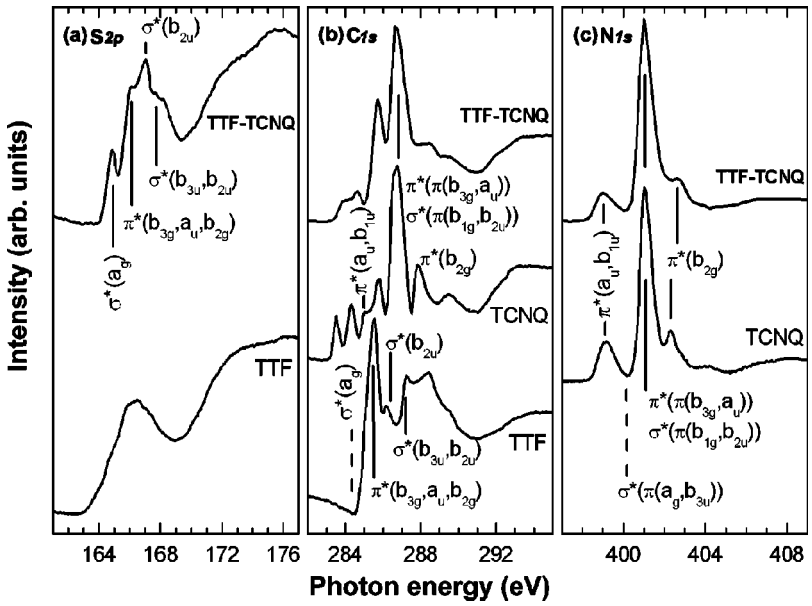

FIG. 7. S2*p*, C1*s*, and N1*s* XANES spectra for the charge transfer compound TTF-TCNQ and for the neutral TTF and TCNQ.

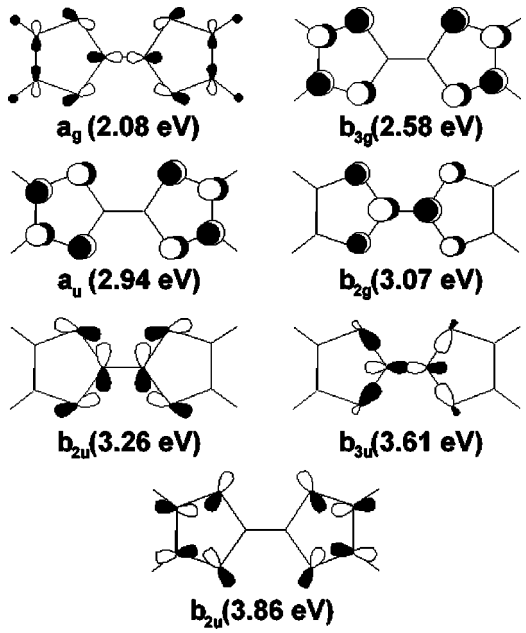

FIG. 8. Schematic representation of the relevant TTF unoccupied molecular orbitals for the analysis of the XANES spectra of TTF and TTF-TCNQ. The symmetry labels are those appropriate for the D_{2h} symmetry. The energy values given (in eV) are relative to those of the HOMO of TTF in the isolated TTF molecule.

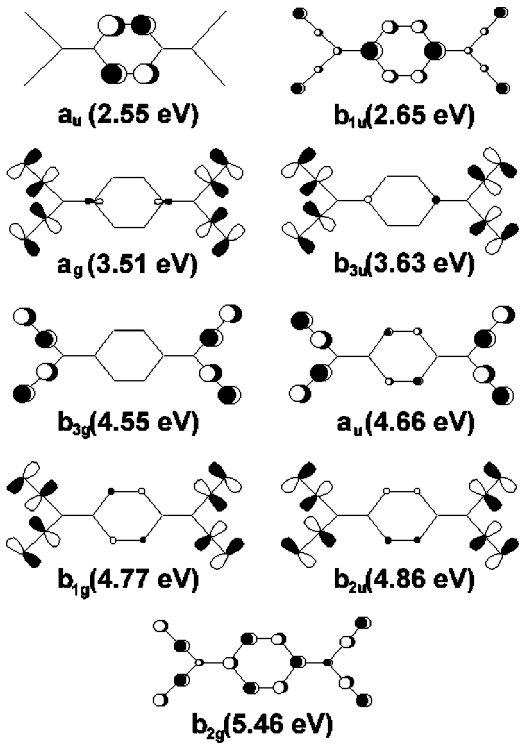

FIG. 9. Schematic representation of the relevant TCNQ unoccupied molecular orbitals for the analysis of the XANES spectra of TCNQ and TTF-TCNQ. The symmetry labels are those appropriate for D_{2h} symmetry. The energy values given (in eV) are relative to those of the LUMO of TCNQ in the isolated TCNQ molecule.

crease of the core-hole lifetime in the excited state that occurs when charge is transferred to form the salt. Since the charge is transferred from the TTF HOMO, which mainly derives from the sulfur atoms as mentioned before [see Fig. 4(d)], the line narrowing is specially important in the S2p XANES. This is thus a rather direct but qualitative method to experimentally determine the influence of charge transfer on the unoccupied electronic states close to the Fermi level.

The calculated DOS and the C and S PDOS of TTF can be quite simply understood. Let us note that for the energy region of interest here, i.e., up to approximately 5–6 eV, the C PDOS is clearly dominated by the *p*-type contributions with the *s*- and *d*-type contributions being much smaller. However, for the S PDOS the weight of the *d*-type contributions become considerably larger. In fact, the *d* contributions extend over all the energy range of interest so that even if the *p* contributions dominate, there is always some *d* contribution of the appropriate symmetry and the levels are going to be visible in some degree in the S2p spectra.

The first unoccupied peak in the total DOS of neutral TTF [see Fig. 4(d)] lies around 2 eV of the TTF HOMO peak. Analysis of the PDOS shows that it is about two thirds S based and one third C based [note the different scales for each PDOS in Fig. 4(d)]. This peak originates from the a_g orbital (see Fig. 8), a σ-type orbital, which is essentially antibonding for all C-S bonds and to a lesser extent between all C-H bonds. The reason why it is the lowest lying empty orbital is that it mixes in C-C bonding contributions thus making the level less antibonding. The main character is C-S antibonding and this orbital will be labeled as σ^* (a_g) and is noted in Fig. 7(a) for charged TTF, where it is clearly observed. This feature is not observed in the C1s XANES spectrum of TTF [dashed line in Fig. 7(b)] as if transitions from an initial *s*-state to a final $\sigma^*(a_g)$-state were forbidden (see more about this later).

The next peak in the DOS of TTF [see Fig. 4(d)], which is the most prominent one, is really the superposition of two contributions, a larger one at around 2.5 eV above the HOMO maximum and a smaller one, appearing as a shoulder slightly below. This is also the case for the C and S PDOS. The two contributions originate from π-type orbitals of TTF. The lower contribution originates from the b_{3g} orbital lying at 2.58 eV from the TTF HOMO (see Fig. 8). The large peak slightly above originates from the pair of a_u and b_{2g} orbitals in Fig. 8, which in the molecule are very near in energy (i.e., at 2.94 and 3.07 eV from the HOMO) and thus appear as a single peak in the DOS. The associated feature will be labeled as $\pi^*(b_{3g},a_u,b_{2g})$, and it can be observed in the XANES curves for both S2p (since it has a significant *d* character in the S atoms) and C1s ($s\rightarrow\pi^*$ transitions in C are allowed) spectra.

The next three peaks in the DOS [see Fig. 4(d)] (seen as two peaks and a shoulder) are due to σ-type orbitals. The first one is due to the lower b_{2u} orbital of Fig. 8, which lies at 3.26 eV from the HOMO in the molecule and is another antibonding C-S level which will be labeled $\sigma^*(b_{2u})$. The two next peaks originate from two orbitals which are quite similar in energy in the molecule: the b_{3u} and upper b_{2u} orbitals of Fig. 8, which lie at 3.61 and 3.86 eV from the HOMO in the molecule. These two orbitals are also

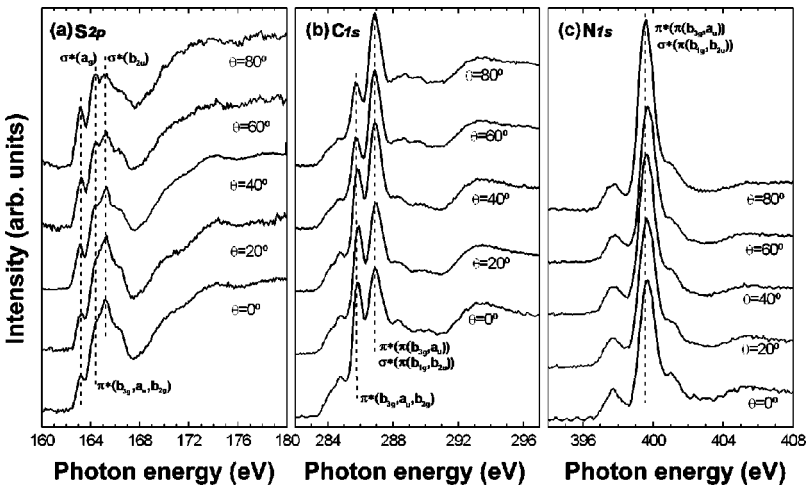

FIG. 10. Angular dependent XANES spectra of TTF-TCNQ for (a) S2p, (b) C1s, and (c) N1s. The θ angle is defined as the angle between the light polarization vector and the surface plane.

C-S antibonding but include also some C-C antibonding character and will be termed as $\sigma^*(b_{3u},b_{2u})$. Note that for the C1s spectrum of neutral TTF the $\sigma^*(b_{2u})$ and $\sigma^*(b_{3u},b_{2u})$ orbitals are clearly observed although we suspect that in the latter case it is mostly because of the b_{2u} contribution and that transitions from an initial s state to a final $\sigma^*(b_{3u})$ state are also forbidden (see below the discussion of the N1s spectra of TCNQ).

It is important to note that although not shown in Fig. 8, the lower b_{2u} orbital contains a sizeable contribution of the appropriate symmetry adapted combination of d_{z^2} orbitals of the S atoms. This is not the case for any of the orbitals considered up to now. This observation will be important in order to understand the angular variation of the S2p spectra. A similar analysis of the higher energy region of the DOS, which contains different $\sigma^*_{\text{C-S}}$, $\sigma^*_{\text{C-C}}$, and $\sigma^*_{\text{C-H}}$ contributions, will not be pursued here since the spectra do not exhibit too much structure. Our S2p XANES spectra of TTF-TCNQ [Fig. 7(a)] closely resembles the S2p inelastic electron scattering spectra from Ristko *et al.*[10] However, in that work no individual assignment to the experimental features is done and on the basis of semiempirical type calculations it is argued that the orbitals involved exhibit b_{3u}, b_{2u}, a_{1g}, and b_{1g}, symmetries, only in partial agreement with the present work.

The origin of the different peaks of the TTF-TCNQ S PDOS [Fig. 6(b)] can be understood exactly as for the neutral TTF [Fig. 4(d)]. This is not that surprising since the TTF 1D stacks in the two solids are very similar and TCNQ does not possess S atoms. Summarizing, the first peaks above the Fermi level in the S PDOS of Fig. 6(b) (note that the third and fourth peaks almost collapse into a single one) originate, respectively, from $\sigma^*(a_g)$, $\pi^*(b_{3g},a_u,b_{2g})$ (the two peaks which were seen as a peak and a shoulder for TTF appear as a single peak now), $\sigma^*(b_{2u})$, and $\sigma^*(b_{3u},b_{2u})$ (which now appear as separate peaks) orbitals of TTF [see Fig. 7(a)]. The differences found in the energies of the peaks in the XANES spectra compared with the peaks in the calculated PDOS are in part due to the fact that the calculated PDOS corresponds to the electronic structure of the ground state while the XANES spectra to the excited-state with a core hole.[39] Discrepancies in intensities may arise from (i) neglecting the S2p spin-orbit splitting in the calculations, (ii) the experimental geometry (relative position of **E** with the molecular orbitals), and (iii) to unidentified selection rules (see discussion below).

Figure 10 shows the XANES spectra as a function of the incidence angle θ for the oriented TTF-TCNQ films. For $\theta=0°$ and θ close to 90° **E** lies parallel and perpendicular to the molecular *ab* plane, respectively. The planar geometry of both TTF and TCNQ molecules will strongly simplify the analysis. The most relevant trends in Fig. 10(a), corresponding to the S2p spectra, are the intensity reduction of the $\sigma^*(b_{2u})$ and the increase of $\sigma^*(a_g)$ with increasing θ. According to the geometry of the TTF molecules and their molecular orbitals (see Figs. 1 and 8), the absorption intensity should exhibit a maximum when the light electric field coincides with the molecular plane, i.e., for large θ values. This is indeed observed for the $\sigma^*(a_g)$, but not for $\sigma^*(b_{2u})$. The reason for this behavior is that, as pointed out earlier, the $\sigma^*(b_{2u})$ feature exhibits significant d_{z^2} contribution, an orbital pointing perpendicularly to the TTF molecular plane (Fig. 1). Since the normal of this molecular plane forms an angle of about 60° with the direction perpendicular to the *ab* plane (c^* direction), the d_{z^2} contribution to the XANES spectrum would be more evident for lower θ values and should be strongly reduced for large θ values, as experimentally observed. Similarly to the $\sigma^*(b_{2u})$ feature, $\pi^*(b_{3g},a_u,b_{2g})$ should decrease at larger values of θ because of the orbital distribution. This behavior is not evident from the spectra because of the overlap with $\sigma^*(b_{2u})$ but the intensity ratio between $\pi^*(b_{3g},a_u,b_{2g})$ and $\sigma^*(a_g)$ decreases for increasing θ values, as expected.

2. TCNQ-derived spectral features

Let us now consider the neutral and charged TCNQ. Both the C1s and N1s spectra are quite well resolved [see Figs. 7(b) and 7(c)]. The PDOS of both N and C in the region of interest here are almost completely dominated by the p-type contributions. Looking at the TCNQ DOS in Fig. 5(d) we can see four clear peaks above that of the LUMO band. The first peak, appearing at around 2.8 eV above the LUMO minimum, originates from the lower a_u and the b_{1u}

orbitals of TCNQ (see Fig. 9), which for the isolated molecule lie at 2.55 and 2.65 eV from the LUMO. These π-type orbitals $\pi^*(a_u, b_{1u})$ are quite strongly concentrated on the benzenic region (small contributions are not shown in the schematic representations of Fig. 9). These orbitals originate from the degenerate pair of lowest empty π orbitals (e_{2u}) of benzene,[40] which only slightly delocalize towards the substituent in TCNQ. The next two peaks are associated to the CN groups. The first one contains the contribution of the bands based on the a_g and b_{3u} orbitals of TCNQ lying at 3.51 and 3.63 eV from the LUMO, and will be labeled $\sigma^*[\pi(a_g, b_{3u})]$ (see the next paragraph for notation), while the second peak contains the contribution of bands based on four orbitals of TCNQ lying at 4.55 (b_{3g}) and 4.66 eV (a_u), labeled as $\pi^*[\pi(b_{3g}, a_u)]$, and 4.77 (b_{1g}) and 4.86 eV (b_{2u}), labeled as $\sigma^*[\pi(b_{1g}, b_{2u})]$, from the LUMO (see Fig. 9). Essentially, the $\pi^*(a_g, b_{3u})$ and $\pi^*(b_{1g}, b_{2u})$ orbitals are the four symmetry adapted combinations of the in-plane π^* orbitals of the CN groups.

It is important to distinguish between the two π^* orthogonal orbitals of the CN group. They are degenerate for CN itself because of the cylindrical symmetry but become nondegenerate in TCNQ. Because of the symmetry plane of the molecule, the two formally degenerate orbitals lead to one in-plane π^* orbital, denoted as $\sigma^*(\pi)$ because it is an antibonding orbital which is symmetrical with respect to the molecular plane even if locally it is a π-type orbital, and one out-of-plane π^* orbital, denoted as $\pi^*(\pi)$ because it is an antibonding orbital which is antisymmetrical with respect to the molecular plane and is locally a π-type orbital. The four $\sigma^*(\pi)$ orbitals lead to four symmetry adapted combinations which are the main components of the four molecular orbitals. Two of them are lower in energy $\sigma^*[\pi(a_g, b_{3u})]$, because they are symmetrical with respect to the C_2 axis along the long molecular axis and they exhibit positive overlap between the C components of the two adjacent $\sigma^*(\pi)$ orbitals. This lowers considerably the energy. The other two orbitals are based on the b_{1g} and b_{2u} orbitals $\sigma^*[\pi(b_{1g}, b_{2u})]$ (see Fig. 9). These orbitals are the two remaining symmetry adapted combinations of the $\sigma^*(\pi)$ orbitals. By having negative overlap between the C component of the two adjacent $\sigma^*(\pi)$ orbitals they lie now around 1 eV higher in energy than their a_g and b_{3u} counterparts (see Fig. 9). The $\pi^*[\pi(b_{3g}, a_u)]$ orbitals are two of the symmetry adapted combinations of the $\pi^*(\pi)$ orbitals. By being symmetrical with respect to the C_2 axis along the long molecular axis, the π orbital of the central C atom of the $C(CN)_2$ substituent cannot mix into these symmetry adapted combinations and thus the $\pi^*(\pi)$ orbitals practically do not delocalize toward the benzene ring.

Before concluding let us note that the next peak, at approximately 5.6 eV from the LUMO minimum, arises from a π-type orbital delocalized all over the molecule but originating from the highest π-type orbital of benzene (b_{2g}).[40] Superposed to this contribution there is a second one, of σ type and also localized on the benzene moiety, whose main character is $\sigma_{C\text{-}H}$ antibonding. However, since this orbital is of a_g symmetry, we suspect it does not lead to any feature in the experimental spectra (see below). Thus, the first and forth peaks are considerably more concentrated in the benzene ring whereas all other peaks are strongly based on π^*_{CN} orbitals. This is clear from the comparison of the C and N PDOS. The higher energy region of the DOS contains the contributions of several quite delocalized σ-type orbitals containing $\sigma^*_{C\text{-}C}$, $\sigma^*_{C\text{-}H}$, and $\sigma^*_{C\text{-}N}$ contributions, the lowest one of which leads to the next feature in the TCNQ spectra, whose analysis will not be pursued here.

The origin of the different peaks of the N PDOS of TTF-TCNQ [Fig. 6(b)] can be understood exactly as for the neutral TCNQ [Fig. 5(d)]. As noted in the discussion of the band structure, there are really no structural reasons for this, but the molecular nature of TCNQ and TTF-TCNQ makes that the differences in the packing do not induce differences in the band topology, which lead to noticeable changes in the DOS. Again, small variations in energy differences between some of the peaks in TCNQ and TTF-TCNQ arise from the differential effect induced by the charge transfer (and to a minor degree from the structural differences). The origin of the peaks for the C1*s* and N1*s* spectra of TCNQ is shown in Figs. 7(b) and 7(c), respectively. Note that the contribution of $\sigma^*[\pi(a_g, b_{3u})]$, which should appear [see the dotted line in Fig. 7(c)] in between those of $\pi^*(a_u, b_{1u})$ and $\pi^*[\pi(b_{3g}, a_u)] + \sigma^*[\pi(b_{1g}, b_{2u})]$, both clearly visible in the N1*s* spectra, does not appear at all. That, the larger peak in the N1*s* spectra is partially associated with $\sigma^*[\pi(b_{1g}, b_{2u})]$ is clear not only from the energy separation from the first peak but, more importantly, from the angular dependence of the peaks, as discussed next.

Figures 10(b) and 10(c) show the angular dependence of the C1*s* and N1*s* XANES spectra, respectively. The most salient feature of Fig. 10(c) is the intensity increase of the $\pi^*[\pi(b_{3g}, a_u)] + \sigma^*[\pi(b_{1g}, b_{2u})]$ peak for increasing θ values. However, the benzenic-type $\pi^*(a_u, b_{1u})$ and $\pi^*(b_{2g})$ peaks remain nearly unchanged. For TCNQ the C_2 molecular axis forms an angle of about 36° with the c^* direction. Since CN bonds form an angle of 60° with this C_2 molecular axis within the molecular plane [see Fig. 1(a)], the intensity associated to $\sigma^*[\pi(b_{3g}, a_u)]$ should increase for larger θ. However, the intensity associated to $\pi^*(\pi)$ orbitals, the benzeniclike orbitals and $\pi^*[\pi(b_{3g}, a_u)]$, should exhibit the opposite behavior because they are perpendicular to the $\sigma^*(\pi)$ orbitals. From Fig. 10(c) it is clear that the $\pi^*[\pi(b_{3g}, a_u)] + \sigma^*[\pi(b_{1g}, b_{2u})]$ peak increases with regard to the benzenic-type orbitals for increasing θ values because of the increasing $\sigma^*(\pi)$ and decreasing $\pi^*(\pi)$ contributions. The same arguments apply for the $\pi^*[\pi(b_{3g}, a_u)] + \sigma^*[\pi(b_{1g}, b_{2u})]$ C1*s* peak [Fig. 10(b)], which indeed increases for increasing θ angles. In the case of TTF $\pi^*(b_{3g}, a_u, b_{2g})$ [Fig. 10(a)], its intensity decreases for increasing θ angles, which is again ascribed to the π character of the bonds as pointed out earlier [see discussion above for S2*p* XANES spectra and note that in Fig. 10(b) the intensity decrease is more readily patent than in the S2*p* case of Fig. 10(a) because of reduced overlap].

In view of these observations we are quite confident on the appropriateness of the assignations in the N1*s* spectra of

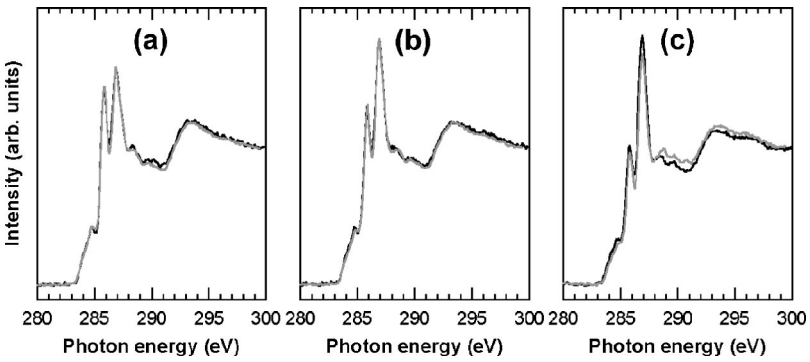

FIG. 11. C1*s* XANES spectra of TTF-TCNQ taken at incidence angles (a) $\theta=0°$, (b) $\theta=40°$, and (c) $\theta=70°$. Black and gray lines correspond to 300 and 10 K, respectively.

Fig. 7(c). This leads to the intriguing observation of the absence of the $\sigma^*[\pi(a_g,b_{3u})]$ contribution in the N1*s* XANES spectra of both neutral TCNQ and TTF-TCNQ. Let us now note the absence of precisely the a_g and b_{3u} contributions in the C1*s* spectra of TTF discussed above. However, the C1*s* XANES spectrum of TCNQ shows some intensity in the $\sigma^*[\pi(a_g,b_{3u})]$ region (between $\pi^*(a_u,b_{1u})$ and $\pi^*[\pi(b_{3g},a_u)]+\sigma^*[\pi(b_{1g},b_{2u})]$). This is due to the significant *d* contribution from carbon for neutral TCNQ while nitrogen contributes negligibly. Thus, it seems that in addition to the intraatomic selection rules there are additional restrictions behind the possibility of observation of certain features of the DOS in molecular materials like those discussed here. We have no appropriate explanation for this interesting observation which certainly calls for both theoretical and experimental additional work (for instance the detailed comparison of the N1*s* XANES spectra of appropriate mono- and di-cyanosubstituted systems could bring some light into this problem). Our molecular orbital assignation to the N1*s* XANES spectra differs from that of Ritsko *et al.*[10] mainly because of their lower experimental resolution, which results in a single peak in the inelastic electron scattering spectra, which they assign to have b_{3u}, a_{1g}, and a_{1u} symmetry. Additionally, the origin of the two lower energy C1*s* XANES features (at around 284 eV) for both neutral TCNQ and TTF-TCNQ is also uncertain. No peaks are associated in the predicted PDOS in this region [see Figs. 5(d) and 6(b)] and no instrumental artifacts are expected (i.e., higher-order light from the monochromator). Contribution from interfacial states [at the TTF-TCNQ / KCl(100) interface], which can be clearly distinguished in XANES spectra,[41] can be ruled out because of the large film thickness (around 1 μm). The presence of both peaks might be related to the excited state nature of the absorption process but we are unable to be more precise on this point.

Figure 11 shows the C1*s* XANES spectra taken at different incidence angles (0°, 40°, and 70°) and measured at 10 and 300 K, respectively. No relevant changes are observed upon undergoing the Peierls transition ($\sim$55 K), except for large values of θ, evidencing that XANES mainly explores the molecular contribution to the electronic structure. This is in line with XANES experiments on perylene crystals, where the spectra look very similar for both α and β polymorphs, which exhibit differentiated structures.[41] The conduction barrier energy or activation energy Δ of the films is $\Delta>30$ meV as determined from resistivity measurements and the Peierls transition has been only observed for TTF-TCNQ films with $\Delta<25$ meV. The reduction of Δ is intimately related to the reduction of the grain boundary density.[15]

C. Electronic structure of occupied states

The electronic structure of the occupied states of TTF-TCNQ has been experimentally determined for single crystals[7–9] and thin films prepared under the same conditions as those reported here[42] by means of ARPES performed at sample temperatures below 100 K. In the case of single crystals dispersion along the Γ-*Y* direction is clearly observed together with extremely low spectral intensity at the Fermi level, a common property of quasi-1D materials.[43] Due to the surface stability of oriented thin TTF-TCNQ films in air, *ex situ* grown films do also exhibit band dispersion. In addition to the 60 meV pseudogap already observed in the metallic phase in the single crystal samples about 50 meV shift is observed due to contamination and nonstoichiometry at grain boundaries. In thin films the band dispersion is also observed, even with the overlap of both *a* and *b* directions in the films (see Sec. II), because of the shape of the band surface in reciprocal space, which may be approximated by a sheet in *E* vs Γ-*X*, Γ-*Y* space with $\partial E/\partial k_{a*}=0$ and $\partial E/\partial k_{b*}\neq 0$, where *E* represents the band energy and k_{a*} and k_{b*} stand for the wave vectors along a^* and b^* directions, respectively.[44] The x-ray photoelectron spectroscopy (XPS) analysis of single crystals and films reveals that charged and neutral TCNQ may coexist at the surface, either dynamically, if the conversion period is larger than the characteristic time of the photoexcitation process, or static, in the case of incomplete charge transfer or contamination.[9,42] The coexistence of bulk charged and neutral species has been confirmed for the quasi-1D organic conductor diperylene hexafluorophosphate as determined by high-resolution nuclear magnetic resonance (NMR).[45] In the case of thin films neutral TCNQ is probably allocated at grain boundaries. Band dispersion is only observed at cryogenic temperatures because of the considerable vibration of the surface molecules in ultrahigh vacuum at room temperature. These surface thermal vibrations, caused by a small surface Debye temperature, smaller than 160 K, the bulk value,[46] induce a reduction of ρ. According to our band calculations [see Fig. 5(c)] neutral TCNQ should contribute with energy states at about 0.8 eV binding energy (the Fermi level is taken half-

way of the HOMO-LUMO gap). A band at this energy is found for both TTF-TCNQ single crystals and thin films.

The ARPES spectra may be thus divided in three regions (i) $0 \leqslant E \leqslant 0.5$ eV, (ii) $E \sim 0.8$ eV, and (iii) $E \sim 1.5$ eV. Regions (i) and (iii) agree with most of band calculations[8,29,30] including the present work and discrepancies arise when considering region (ii). If the 0.8 eV peak could be ascribed to the presence of neutral TCNQ on the surface, the only major contribution from the one dimensionality would be the strong reduction of electronic states at the Fermi level. In our opinion the separation of spin-charge suggested by Claessen *et al.*[8] cannot be concluded only from the ARPES experiments.

V. CONCLUSIONS

The electronic structure of the unoccupied states of neutral TTF and TCNQ as well as of the quasi-1D charge transfer salt TTF-TCNQ has been experimentally determined by means of XANES and compared to DFT calculations. Since the intermolecular interactions are weak the electronic structure of molecular solids is mainly determined by the molecular character, so that the energy levels are essentially given by the molecular orbital energies. The use of synchrotron radiation allows the determination of the PDOS because of the element selectivity of x-ray absorption and the determination of the spatial distribution of the molecular orbitals due to the polarization of the synchrotron light. State of the art DFT computations have been used to calculate the band structure, DOS, and PDOS of TTF, TCNQ, and TTF-TCNQ. The partially filled bands of the 1D metal TTF-TCNQ have been characterized and then compared with recent theoretical studies. An in depth discussion of the origin of the different features of the unoccupied DOS of the three materials, TTF, TCNQ, and TTF-TCNQ, has been possible. The combined experiment-theory study has permitted the assignation of most of the experimentally obtained features to molecular orbitals of specific energy and symmetry. Thus, a complete description of the nature of the states from the Fermi level up to approximately 6 eV above is obtained. It is observed that the contributions associated with molecular orbitals of specific symmetry (a_g and b_{3u} in D_{2h}) are not observed in the XANES spectra, despite being clearly visible in the calculated DOS. This suggests that there are selection rules still not well understood for materials structurally as complex as TTF, TCNQ, and TTF-TCNQ. More work on carefully chosen molecular materials (i.e., based on molecules with symmetry lower than D_{2h}) is clearly needed in order to progress along these lines.

ACKNOWLEDGMENTS

The work at HUT was supported by the Academy of Finland through the Center of Excellence Program (2002-2005). Work at Bellaterra was supported by DGI-Spain (Projects No. MAT1999-1128 and BFM2000-1312-C02-01), Generalitat de Catalunya (2001 SGR 33), and by grants for computer time from the CESCA-CEPBA. Regarding synchrotron work, we are indebted to P. Parent and C. Laffon for their help with the measurements at LURE and to L. J. Terminello for helping with the SSRL experiments. The SSRL is funded by the US-DOE, Office of Basic Energy Science. The synchrotron work at LURE was financed by the TMR Program of the European Union.

[1] J. Ferraris, D.O. Cowan, V.V. Walatka, and J.H. Perlstein, J. Am. Chem. Soc. **95**, 948 (1973); L.B. Coleman, M.J. Cohen, D.J. Sandman, F.G. Yamagishi, A.F. Garito, and A.J. Heeger, Solid State Commun. **12**, 1125 (1973).

[2] T. Ishiguro, K. Yamaji, and G. Saito, *Organic Superconductors*, 2nd ed. (Springer-Verlag, Berlin, 1998).

[3] T.J. Kistenmacher, T.E. Philips, and D.O. Cowan, Acta Crystallogr., Sect. B: Struct. Crystallogr. Cryst. Chem. **30**, 763 (1974).

[4] E.M. Conwell in *Semiconductors and Semimetals*, edited by E. Conwell (Academic Press, New York, 1988), Vol. 27, p. 215.

[5] D. Jérome and H. Schulz, Adv. Phys. **31**, 299 (1982).

[6] D. Jérome, A. Mazaud, M. Ribault, and K. Bechgaard, J. Phys. (France) Lett. **41**, L-95 (1980).

[7] F. Zwick, D. Jérome, G. Margaritondo, M. Onellion, J. Voit, and M. Grioni, Phys. Rev. Lett. **81**, 2974 (1998).

[8] R. Claessen, M. Sing, U. Schwingenschlögl, P. Blaha, M. Dressel, and C.S. Jacobsen, Phys. Rev. Lett. **88**, 096402 (2002).

[9] M. Sing, U. Schwingenschlögl, R. Claessen, M. Dressel, and C.S. Jacobsen, Phys. Rev. B **67**, 125402 (2003).

[10] J.J. Ritsko, N.O. Lipari, P.C. Gibbons, and S.E. Schnatterly, Phys. Rev. Lett. **37**, 1068 (1976).

[11] W. Gebauer, M. Bassler, R. Fink, M. Sokolowski, and E. Umbach, Chem. Phys. Lett. **266**, 177 (1997); J. Poppensieker, Ch. Röthig, and H. Fuchs, Adv. Funct. Mater. **11**, 188 (2001).

[12] J. Stöhr, *NEXAFS Spectroscopy* (Springer, Berlin, 1992).

[13] A. Curioni, W. Andreoni, R. Treusch, F.J. Himpsel, E. Haskal, P. Seidler, C. Heske, S. Kakar, T. Van Buuren, and L.J. Terminello, Appl. Phys. Lett. **72**, 1575 (1998).

[14] A. Bianconi, S.B.M. Hagstrom, and R.Z. Bachrach, Phys. Rev. B **16**, 5543 (1977); J. Fraxedas, A. Stampfl, R.C.G. Leckey, J.D. Riley, and L. Ley, Phys. Rev. B **42**, 8966 (1990).

[15] J. Fraxedas, S. Molas, A. Figueras, I. Jiménez, R. Gago, P. Auban-Senzier, and M. Goffman, J. Solid State Chem. **168**, 384 (2002).

[16] R.A. Rosenberg, P.J. Love, and V. Rehn, Phys. Rev. B **33**, 4034 (1986).

[17] A.M. Bradshaw and N.V. Richardson, Pure Appl. Chem. **68**, 457 (1996).

[18] P. Hohenberg and W. Kohn, Phys. Rev. **136**, 864 (1964); W. Kohn and L.J. Sham, *ibid.* **140**, 1133 (1965).

[19] P. Ordejón, E. Artacho, and J.M. Soler, Phys. Rev. B **53**, R10441 (1996); D. Sánchez-Portal, P. Ordejón, E. Artacho, and J.M. Soler, Int. J. Quantum Chem. **65**, 453 (1997); J.M. Soler, E. Artacho, J.D. Gale, A. Garcia, J. Junquera, P. Ordejon, and D. Sanchez-Portal, J. Phys.: Condens. Matter **14**, 2745 (2002).

[20] J.P. Perdew, K. Burke, and M. Ernzerhof, Phys. Rev. Lett. **77**, 3865 (1996).

[21] N. Trouiller and J.L. Martins, Phys. Rev. B **43**, 1993 (1991).
[22] L. Kleinman and D.M. Bylander, Phys. Rev. Lett. **48**, 1425 (1982).
[23] S.G. Louie, S. Froyen, and M.L. Cohen, Phys. Rev. B **26**, 1738 (1982).
[24] E. Artacho, D. Sánchez-Portal, P. Ordejón, A. Garcia, and J.M. Soler, Phys. Status Solidi B **215**, 809 (1999).
[25] H.J. Monkhorst and J.D. Pack, Phys. Rev. B **13**, 5188 (1976).
[26] Y.J. Lee, R.M. Nieminen, P. Ordejón, and E. Canadell, Phys. Rev. B **67**, 180505(R) (2003).
[27] E.B. Starikov, Solid State Commun. **91**, 45 (1994).
[28] R.V. Kasowski, M.-H. Tsai, S.T. Chui, and J.D. Dow, Phys. Rev. B **46**, 10017 (1992).
[29] S. Ishibashi and M. Kohyama, Phys. Rev. B **62**, 7839 (2000).
[30] M. Sing, R. Claessen, Th. Finteis, S. Hao, S. Hüfner, and P. Blaha, J. Electron Spectrosc. Relat. Phenom. **114-116**, 717 (2001).
[31] C.S. Jacobsen, Mat. Fys. Medd. K. Dan. Vidensk. Selsk. **41**, 251 (1985).
[32] A.J. Schultz, G.D. Stucky, R.H. Blessing, and P. Coppens, J. Am. Chem. Soc. **98**, 3194 (1976).
[33] A. Filhol, G. Bravic, J. Gaultier, D. Chasseau, and C. Vettier, Acta Crystallogr., Sect. B: Struct. Crystallogr. Cryst. Chem. **37**, 1225 (1981).
[34] J.P. Pouget, in *Semiconductors and Semimetals*, edited by E. Conwell (Academic, New York, 1988), Vol. 27, p. 88.
[35] Z.Z. Wang, J.C. Girard, C. Pasquier, D. Jérome, and K. Bechgaard, Phys. Rev. B **67**, 121401 (2003).
[36] W.F. Cooper, N.C. Kenney, J.W. Edmons, A. Nagel, F. Wudl, and P. Coppens, Chem. Commun. (Cambridge) **1971**, 889.
[37] R.E. Long, R.A. Sparks, and K.N. Trueblood, Acta Crystallogr. **18**, 932 (1965).
[38] A. Barrie, I.W. Drummond, and Q.C. Herd, J. Electron Spectrosc. Relat. Phenom. **5**, 217 (1974).
[39] E.L. Shirley, Phys. Rev. Lett. **80**, 794 (1998).
[40] T.A. Albright, J.K. Burdett, and M.-H. Whangbo, *Orbital Interactions in Chemistry* (John Wiley & Sons, New York, 1985).
[41] J. Taborski, P. Vaterlein, H. Dietz, U. Zimmermann, and E. Umbach, J. Electron Spectrosc. Relat. Phenom. **75**, 129 (1995).
[42] C. Rojas, J. Caro, M. Grioni, and J. Fraxedas, Surf. Sci. **482-485**, 546 (2001).
[43] S.F. Lin, W.E. Spicer, and B.H. Schechtman, Phys. Rev. B **12**, 4184 (1975); C. Coluzza, H. Berger, P. Alméras, F. Gozzo, G. Margaritondo, G. Indlekofer, L. Forro, and Y. Hwu, *ibid.* **47**, 6625 (1993); K.E. Smith, Annu. Rep. Prog. Chem., Sect. C: Phys. Chem. **90**, 115 (1993).
[44] J. Fraxedas, H.J. Trodahl, S. Gopalan, L. Ley, and M. Cardona, Phys. Rev. B **41**, 10068 (1990).
[45] G. Fischer and E. Dormann, Phys. Rev. B **58**, 7792 (1998).
[46] K. Saito, Y. Yamamura, H. Akatsu, M. Takeda, H. Asaoka, H. Nishikawa, I. Ikemoto, and M. Sorai, J. Phys. Soc. Jpn. **68**, 1277 (1999).